Title
Impacts of Mixed-Wettability on Brine Drainage and Supercritical CO2 Storage Efficiency in a 2.5-D Heterogeneous Micromodel

Journal
Water Resources Research, 56(7)

ISSN
0043-1397

Authors
Chang, C
Kneafsey, TJ
Wan, J
et al.

Publication Date
2020-07-01

DOI
10.1029/2019WR026789

Peer reviewed

Impacts of Mixed-Wettability on Brine Drainage and Supercritical CO_2 Storage Efficiency in a 2.5-D Heterogeneous Micromodel

Chun Chang[*], Timothy J. Kneafsey, Jiamin Wan, Tetsu K. Tokunaga, Seiji Nakagawa

Energy Geosciences Division, Lawrence Berkeley National Laboratory, Berkeley, CA 94720, USA.

[*]Corresponding author. *E-mail address*: chunchang@lbl.gov

Key points

1. We created two mixed-wet systems with varying water- and intermediate-wet patches in a 2.5-D heterogeneous micromodel;
2. The uniformly distributed intermediate-wet patches yield bridging flow topology and highest storage efficiency after drainage;
3. The heterogeneously distributed intermediate-wet patches enhance channelized CO_2 flow and hinder storage efficiency after drainage.

Abstract: Geological carbon storage (GCS) involves unstable drainage processes, the formation of patterns in a morphologically unstable interface between two fluids in a porous medium during drainage. The unstable drainage processes affect CO_2 storage efficiency and plume distribution, and can be greatly complicated by the mixed-wet nature of rock surfaces common in hydrocarbon reservoirs where supercritical CO_2 ($scCO_2$) is used in enhanced oil recovery. We performed $scCO_2$ injection (brine drainage) experiments at 8.5 MPa and 45 °C in heterogeneous micromodels, two mixed-wet with varying water- and intermediate-wet patches, and one water-wet. The flow regime changes from capillary fingering through crossover to viscous fingering in the micromodels of same pore geometry but different wetting surfaces at displacement rates with *logCa* (capillary number) increasing from −8.1 to −4.4. While the mixed-wet micromodel with uniformly distributed intermediate-wet patches yields ~0.15 $scCO_2$ saturation increase at both capillary fingering and crossover flow regimes ($-8.1 \leq logCa \leq -6.1$), the one heterogeneous wetting to $scCO_2$ results in ~0.09 saturation increase only at the crossover flow regime ($-7.1 \leq logCa \leq -6.1$). The interconnected flow paths in the former are quantified and compared to the channelized $scCO_2$ flow through intermediate-wet patches in the latter by topological analysis. At *logCa*>¿ −6.1 (near well), the effects of wettability and pore geometry are suppressed by strong viscous force. Both $scCO_2$ saturation and

distribution suggest the importance of wettability on CO_2 storage efficiency and plume shape in reservoirs, and capillary leakage through caprock at GCS conditions.

1. Introduction

Geological carbon storage (GCS) in subsurface reservoirs has significant capacity for reducing greenhouse gas emissions into the atmosphere (IPCC, 2005). Key questions include (1) the storage efficiency of a geological formation, which is the fraction of the total pore space used by GCS (Bachu et al., 2007; Goodman et al., 2011), and (2) the spread of a CO_2 plume, which needs to be monitored and controlled to ensure safe and permanent storage (Nordbotten et al., 2005; Juanes et al., 2010; Doughty et al., 2010; MacMinn et al., 2010, 2011). Both questions are closely related to the migration of the CO_2 plume during injection, with formation brine (the wetting fluid) displaced by supercritical CO_2 ($scCO_2$, the non-wetting fluid). One of the major reasons for inefficient CO_2 storage in the subsurface is unstable displacement characterized by fingering flow due to the low viscosity of $scCO_2$ relative to formation brine (typical ratio ~1:20) (Zhang et al., 2011a,b; Wang et al., 2012; Berg & Ott, 2012). The unstable displacement and fingering flow of $scCO_2$ will also increase leakage potential through caprock (Tsang et al., 2008), non-equilibrium CO_2 dissolution (Chang et al., 2013, 2014, 2016, 2017, 2019a,b), and mineral trapping (Sanchez-Vila et al., 2007; Huq et al., 2015) after injection ceases.

Unstable displacement can be further complicated by the solid surface wettability. While deep saline aquifers for GCS typically show water-wet behavior, depleted hydrocarbon reservoirs, where $scCO_2$ has been used for enhanced oil recovery and carbon sequestration, can exhibit intermediate-wet or mixed-wet rock surfaces (Salathiel, 1973; Anderson, 1987a,b). It also has been observed the $scCO_2$-induced wettability changes from water-wet to intermediate-wet on rock surface (Yang et al., 2008; Broseta et al., 2012; Jung & Wan, 2012; Seyyedi et al., 2015), in glass micromodels (Kim et al., 2015), and in glass beads and sand pack columns (Tokunaga et al., 2013; Wang & Tokunaga, 2015; Lv et al., 2017). These changes occur in local patches where water films are thin and ionic strengths are high, yielding a mixed-wet system (Kovscek et al., 1993; Jung & Wan, 2012). Many studies have investigated the effects of uniform solid surface wettability (from water-wet to intermediate-wet) on displacement characteristics, non-wetting phase distribution and capillary trapping at the reservoir scale (Al-Khdheeawi et al., 2017), the core scale (e.g., Anderson, 1987a,b; Morrow, 1990; Levine et al., 2014), and the pore scale (Cottin et al., 2011; Zhao et al., 2016; Hu et al., 2017a,b). At the pore scale, flow dynamics of individual oil ganglions have been recently imaged in a single pore/pore throat with mixed-wet solid surfaces by a synchrotron-based X-ray computed tomography (Rücker et al., 2019). The unstable displacement and $scCO_2$ saturation in mixed-wet pore networks remain poorly understood, may greatly complicate the modeling predictions (Celia et al., 2015), and need systematic study.

Two-phase flow and displacement have been widely investigated using two-dimensional (2-D) micromodels monitored with high-resolution optical imaging systems. “2-D” here indicates the pore network has varying pore sizes in the horizontal plane, but has a uniform depth in the vertical dimension. The classic capillary number (Ca), in its original form: $Ca = \mu \times \bar{u} / \sigma$, was used to interpret the fingering geometry in a Hele-Shaw cell by Saffman & Taylor (1958). In this definition, μ is the viscosity of the resident fluid, $\bar{u}$ is the average Darcy velocity of the injected fluid, and σ is the interfacial tension between the injected and resident fluid. Given negligible influences of gravitational forces in thin micromodels, the classic Ca, along with the viscosity ratio (M) defined as the ratio of viscosities of the displacing (non-wetting) and displaced (wetting) fluids, were used to characterize the pore-scale regimes of stable displacement, capillary fingering, viscosity fingering, and their crossover. Different types of micromodels have been developed to investigate the two-phase displacement fundamentals that include (1) homogeneous pore networks composed with regular cubic, cylindrical, elliptical and hexagonal posts (Xu et al., 1998; Ferer et al., 2004; Cottin et al., 2010; Zhang et al., 2011a,b; Wang et al., 2012; Armstrong & Berg, 2013; Chang et al., 2019a,b), (2) heterogeneous pore networks with irregular cylindrical posts (Zarikos et al., 2018), (3) statistically generated pore networks with or without spatial correlation of pore sizes (Tsakiroglou & Avraam, 2002), and (4) heterogeneous pore networks fabricated from a section micrograph of natural consolidated sandstone (Zuo et al., 2013) and transparent cells packed with unconsolidated, single-layered glass beads (Moebius & Or, 2014). Some other studies have reported better description of the pore-scale viscous and capillary forces using modified *Ca* that considers the length scales corresponding to the size of non-wetting phase clusters (Hilfer & Øren, 1996; Armstrong et al., 2014; Chang et al., 2019a). Common to all of the above studies is the use of 2-D geometry of pore network that has a constant pore/pore throat depth. Lacking ability to continuously record in-situ and dynamic interfacial curvature, measured pore widths and depths were used to calculate the capillary pressure using Young-Laplace equation. The dependence of this relation on the sum of the inverse of two orthogonal radii of curvatures shows that constant-depth micromodels effectively fix one of the principal radii, thus limiting the range of capillary pressures achievable through variation of pore widths. The pioneering work from Wan et al. (1996) improved the glass micromodel design and fabrication to provide the necessary contrast of depths (thus capillarity) between matrix pores and fracture apertures. In recent years, more 2.5-D micromodels have been used to better mimic real 3-D porous media and investigate multiphase flow (Park et al., 2015; Yun et al., 2017; Xu et al., 2017a,b). To our best knowledge, there are few studies on unstable drainage processes in micromodels having 2.5-D pore geometry heterogeneity, especially for GCS applications, and none that have examined impacts of mixed wetting.

In this study, we (1) create mixed-wet systems by heterogeneously applying octadecyltrichlorosilane (OTS, 0.2% by vol. in hexane) flow to modify surface wettability of a 2.5-D micromodel in two ways, (2) investigate the $scCO_2$ displacement characteristics and compare the steady-state $scCO_2$ saturations for water-wet and the two types of mixed-wet micromodels; and (3) quantify the $scCO_2$ flow characteristics at both pore- and pore-network scale through a topological analysis. We conducted a series of experiments by injecting $scCO_2$ into an initially brine-saturated micromodel at displacement rates resulting in *logCa* (logarithm of the capillary number) ranging from −8.1 to −4.4, allowing investigation of capillary through viscous fingering (at constant M = 0.038). For simplicity and ease of comparisons with other studies, the first form of the capillary number *Ca* used in this presentation does not include a contact angle term. Later, the capillary number *Ca*¿containing the cosine of the effective contact angle will be introduced for comparison. Images of $scCO_2$ and water distribution were obtained at appropriate junctures to provide direct observations on the pore-scale displacement characteristics and

$scCO_2$ saturation in these pore networks having heterogeneity in both 2.5-D pore geometry and surface wettability.

2. Materials and methods

2.1 2.5-D micromodel

Figure 1(a) shows the 2.5-D pore network contained in a 20 mm ×10 mm rectangle, with a porosity of 0.43 and pore volume of 3.44 μL. The pore network, with pore space shown in white and solid posts in black, was extracted from micro-CT images of sand pack of irregular shaped sand grains, then etched on two symmetrical silica wafers with hydrofluoric acid and then fused together (Micronit Microfluidics BV, Netherlands). The different depths of pores and pore throats were created through etching two mirror image networks, both to 20 μm depths, but with one face having locations left unetched. Thus, 40 μm depth pores are created at locations where both faces were etched to 20 μm, while 20 μm deep throats were created at locations where only one face was etched. Direct aligned bonding of the two plates was then performed by creating a prebond between the two wafers, which was then annealed at high temperature. Given the strong bonding, the micromodel can be operated under the pressure difference (inside relative to outside) up to 10 MPa, without applying any confining pressure as has been required in other high-pressure micromodels (Zhang et al., 2011a; Chang et al., 2016). Figure 1(b) shows the 2-D pore-size distribution (without taking into account the depth of the micromodel) characterized by a local thickness plugin in ImageJ software (Hildebrand and Rüesgsegger, 1996; Rasband, 1997–2019). The average pore and pore-throat size are 190 and 48 μm, respectively, while the average post size is 290 μm.

The pore network also contains a capillary barrier transverse to the flow direction (marked by the yellow lines in Figure 1(a) and 1(c)), composed by a line of tight pore throats 20 μm deep. Figure 1(d) depicts the capillary entry pressure along the capillary barrier, calculated from the pore/pore throat size and depth as follows:

$$p_b = \frac{\sigma cos\theta \left(r_1 + r_2 \right)}{r_1 r_2} \qquad \text{Eq. (1)}$$

Fluid properties		**Displacement rate**		
Pressure	8.5 MPa	Q (μL/min)	$\bar{u}$ (m/d)	*logCa*
Temperature	45 °C	0.1	0.8	-8.1
Viscosity $scCO_2$/water (mPa·s)	0.023/0.597	0.5	4.2	-7.4
Viscosity Hexane/EG (mPa·s)	0.30/16.90	1.0	8.4	-7.1
Interfacial tension (mN/m)	28.5	2.0	16.7	-6.8
Micromodel properties		5.0	41.9	-6.4
Dimension (cm^2)	2.0×1.0	10	83.7	-6.1
Pore volume (μL)	3.44	20	167.4	-5.8
Porosity	0.43	50	418.6	-5.4
Pore/throat depth (μm)	40/20	100	837.2	-5.1
Pore/throat/post diameter (μm)	190/48/290	200	1674.4	-4.8
$scCO_2$/water contact angle	27°	500	4186.0	-4.4

where σ =28.5 mN/m (Chiquet et al., 2007), θ is measured as 27° for $scCO_2$ and brine (see Section 3.1 for more details), r_1 is the local pore radius quantified from Figure 1b and r_2 is the half pore depth. Although

40 μm deep pores are distributed throughout the micromodel, as shown in Figure 1(c) and 1(d), there are only eight of these pores along A-A’ (marked by the red arrows), with the others being 20 μm deep. These eight locations will be referred to as “slots” because they constitute pores with low capillary entry pressures. The impacts of this unique characteristic on $scCO_2$ invasion patterns for water-wet and mixed-wet conditions will be presented in Section 3. Table 1 lists more details on the pore network.

Table 1. Summary of experimental conditions, fluid and micromodel properties, volumetric flow rates, and corresponding Darcy velocities and capillary numbers

Figure 1. (a) Pore characteristics of the 2.5-D micromodel used in this study, with solid posts shown in black, large pores 40 μm deep shown in white and tight pore throats 20 μm deep in red. (b) The pore size distribution quantified by the Local Thickness plugin in ImageJ

software. (c) The sub-image magnified from the red box in (a) that shows the transverse capillary barrier in the pore network. (d) The capillary entry pressure of pores and pore throats for $scCO_2$-water displacement with water-wet solid surface (θ =27°) along the yellow dotted line A–A' shown in (a) and (c). S1 to S8 (marked by the red arrows in (c)) are the open slots in the capillary barrier with reduced capillary entry pressure that may provide potential flow paths for CO_2 invasion. The blue box in (a) and (c) bounds the local pore domain that correlates to the narrow intermediate-wet choke point in Figure 3(c) and constrained $scCO_2$ flow in Figure 4(b). The blue arrow indicates the $scCO_2$ flow direction during the displacement experiments.

2.2 Mixed-wet treatment

Contacting the water-wet glass surface with octadecyltrichlorosilane (OTS) strongly impacts the wettability, changing it towards non-water wetting. The coating solution was prepared by diluting octadecyltrichlorosilane (Cole-Parmer, IL) with hexane (ACS grade, Cole-Parmer, IL) in 4.0%, 0.4% and 0.2% volumetric fractions. Before modifying wettability of the glass micromodel, treatment tests on glass microscope slides were conducted following the sequential steps of (1) acid cleaning, (2) coating in OTS/hexane solution, (3) rinsing in hexane to remove excess OTS, and (4) drying in oven at 100 °C. Contact angle measurements of a water droplet on the microscope slides show values change from 0° to ~75° after treatment by the three concentrated solutions. The contact angle remains constant for over 2 years, indicating the long-term effectiveness of the method (Figure S1 of the supporting information (SI)). The lowest concentrated (0.2% v/v) OTS solution was selected for micromodel treatment to minimize potential effects from the excess OTS. A similar OTS/hexane solution has also been used for changing glass surface wettability in a previous study (Goodwin et al., 2016).

To create a mixed-wet system in the micromodel, we used the OTS/hexane solution as the invading fluid into an ethylene glycol (EG, wetting phase) saturated micromodel. During the treatment, we were able to easily observe the two-phase interface and wettability-altered pore domain because we colored the EG with sulphorhodamine B and collected images of dyed EG distribution under UV light. A low dye concentration (0.23 g/L) was used to minimize its potential effect on fluid viscosity, while allowing sufficient optical detection for phase discernment. The viscosities of the coating solution and dyed EG were assumed equal to that of hexane (0.3 mPa·s) and EG (16.9 mPa·s) due to the low OTS and dye concentration, while the interfacial tension (IFT) between hexane and dyed EG at ambient conditions was measured as 20.5 mN/m through a high-precision tensiometer (Kruss, Germany). Note the close viscosity ratio and IFT between hexane-EG under ambient conditions and $scCO_2$-water system under designated experimental conditions (at 8.5 MPa and 45°C, $\mu_{CO2}=$¿ 0.02 mPa·s, $\mu_{brine}=$¿ 0.6 mPa·s, IFT: 28.5 mN/m). With these similarities, the mixed-wet pattern induced by hexane-based coating solution and EG was expected to be similar to that induced by $scCO_2$-brine at GCS conditions. This was experimentally validated and is presented in Sections 3.2 and 3.3.

During treatment, the micromodel was first acetone cleaned, air dried and then saturated with dyed EG. The surface coating OTS solution was then injected at constant flow rates using a syringe pump (Harvard Apparatus, Holliston, MA). Over 3 and 300 pore volumes (PVs) of coating solution were injected into the micromodel at 3 μL/hour ($logCa=-7.2$) and 6000 μL/hour ($logCa=-3.9$), respectively, until the two-phase distribution in the pore network remained constant with time. After ten displacement experiments with varying injection rates between them using hexane and EG, we selected the minimum and maximum rate injections, which represent potential mixed-wet patterns induced by capillary fingering (minimum rate injection) and viscous fingering (maximum rate injection). Other mixed-wet patterns may vary between them, but we think these two are the boundary cases that worth of detailed investigation. The coating solution injection ceased after soaked for over 20 min in the pore network, followed by 100 PVs of hexane injection to remove excess OTS from the pore network. Finally, the micromodel was air-dried and cured in the oven at 100° for 1 hour, similar to the treatment on microscope glass slides. Fluorescent images were acquired to characterize the mixed-wet patterns using a Sony FDR-AX100 camcorder with a spatial resolution of 4.5 μm/pixel.

2.3 Experimental setup and procedures

A high-pressure, elevated-temperature setup (Figure 2) was built based on Hu et al. (2017b) for scCO_2 displacement experiments in the water-wet and two mixed-wet micromodels. To establish the initially brine-saturated conditions, low pressure gaseous CO_2 was first injected into the micromodel to displace air from the micromodel and tubing. It should be noted that, to avoid corrosion, our “brine” was a low salinity solution (0.01 M NaCl). This brine was then injected from the back-pressure pump to displace and dissolve the gaseous CO_2 through E→D→C→B→F→H. During these steps, the micromodel system was kept at atmospheric pressure. Similar low salinity brine was also used by Hu et al. (2017b), with an aim to minimize any wettability changes induced by salinity and ionic composition (Fathi et al., 2010, Karadimitriou et al., 2019).

The scCO_2 pump was initially filled with wet CO_2 at approximately 5.87 MPa from a source tank (99.99% purity, Airgas) while Valve A connecting scCO_2 pump to the micromodel was closed. The scCO_2 pump was then pressurized up to 8.5 MPa. The pressure in the micromodel and pipeline E→D→C→B→F→G was gradually increased to

8.5 MPa using the back-pressure pump filled with brine, while keeping valve G connecting to the brine pump closed. All fluids were then allowed to equilibrate at 45 °C for over 12 hours. The pressure and temperature represent reservoir conditions at depths of about 1.0 km.

To prepare the mutually saturated brine and $scCO_2$, 200 mL brine was first injected into the high-pressure reactor (see Figure 2), and then pressurized up to 8.5 MPa by CO_2 injection. The reactor containing $scCO_2$ and brine was heated up to 45 °C and stirred for 24 hours. The $scCO_2$-saturated brine was then transferred to the brine pump. Over 100 PVs of $scCO_2$-saturated brine was then injected to completely saturate the micromodel and the pipelines through G→F→B→C→D→E. Displaced fluid was collected in the back-pressure pump, and the micromodel and fluid delivery pipelines were kept constant at 8.5 MPa and 45 °C.

After the above steps were completed, pre-wetted $scCO_2$ in the $scCO_2$ pump was injected into the micromodel at a specific constant flow rate. Displaced brine was collected in the back-pressure pump, which was maintained at a constant withdrawal rate matched to that of the $scCO_2$ injection. In this way, we obtained good experimental reproducibility under the exactly same experimental conditions (see more details in Figure S2 of SI). When the quasi-steady state was reached, i.e., $scCO_2$ distribution and saturation remained constant with time, $scCO_2$ injection was stopped. The micromodel was then flooded with $scCO_2$-saturated brine until no $scCO_2$ was observed, to prepare the micromodel for the next experiment, conducted at a different $scCO_2$ injection rate. This sequence was repeated for a wide range of flow rates. To avoid any contamination effects on the pore surface wettability during the displacement tests, no dye was employed in either the $scCO_2$ or brine. Table 1 lists the imposed volumetric injection rates in the three micromodels. These rates correspond to a range of Darcy velocities from 0.84 m/day to 4190 m/day, and a range of *logCa* from −8.1 to −4.4. The imposed range of injection rates correspond to flow rates at 0.02 to 70 m away from a typical injection well (with an injection rate of one million metric tonnes of $scCO_2$ per year over a screen length of 15 m assuming uniform flow) at a GCS site.

Despite complications that can arise from $scCO_2$-induced wettability alteration such as those noted in the Introduction, we do not expect considerable wettability changes on micromodel surfaces subjected to repeated $scCO_2$ injection because of the relative short time of $scCO_2$ presence in the micromodel (aging time from minutes to hours), and the low ionic strength (0.01M NaCl) used in brine. Hu et al. (2017a,b) also reported constant contact angle measurements before and after repeated $scCO_2$ injection tests, using the same type of silica micromodel (differing only in pore geometry), similar experimental setup, and the same experimental pressure, temperature and brine salinity. Significant wettability changes from brine acidification after

$scCO_2$ dissolution may not be expected from (1) Hu et al. (2017a,b) mentioned above, and (2) Gribanova et al. (1976) who reported that as pH decrease from 6 to 3, contact angles only slightly increased from 19° to 23° in the air−brine−silica system (Gribanova et al., 1976). Nevertheless, it should be recognized that solid surfaces in reservoirs are composed of diverse minerals, where non-uniform chemical interactions (both mineral dissolution and precipitation) and changes of electrochemical properties at brine-rock interface occur, inducing mixed-wet surfaces. These can be further enhanced by the non-uniform $scCO_2$ dissolution and mass transfer in brine, as previously reported (Chang et al., 2017, 2019a). Results from Wang et al. (2013) showed large contact angle variation on different pure mineral surfaces, and analysis suggested that the 38% differences in degrees of contact angle reported could manifest in 5−10% differences in capillary trapping or pressure. In this study, we further show the considerable changes of $scCO_2$ saturation after drainage by the mixed-wet solid surface.

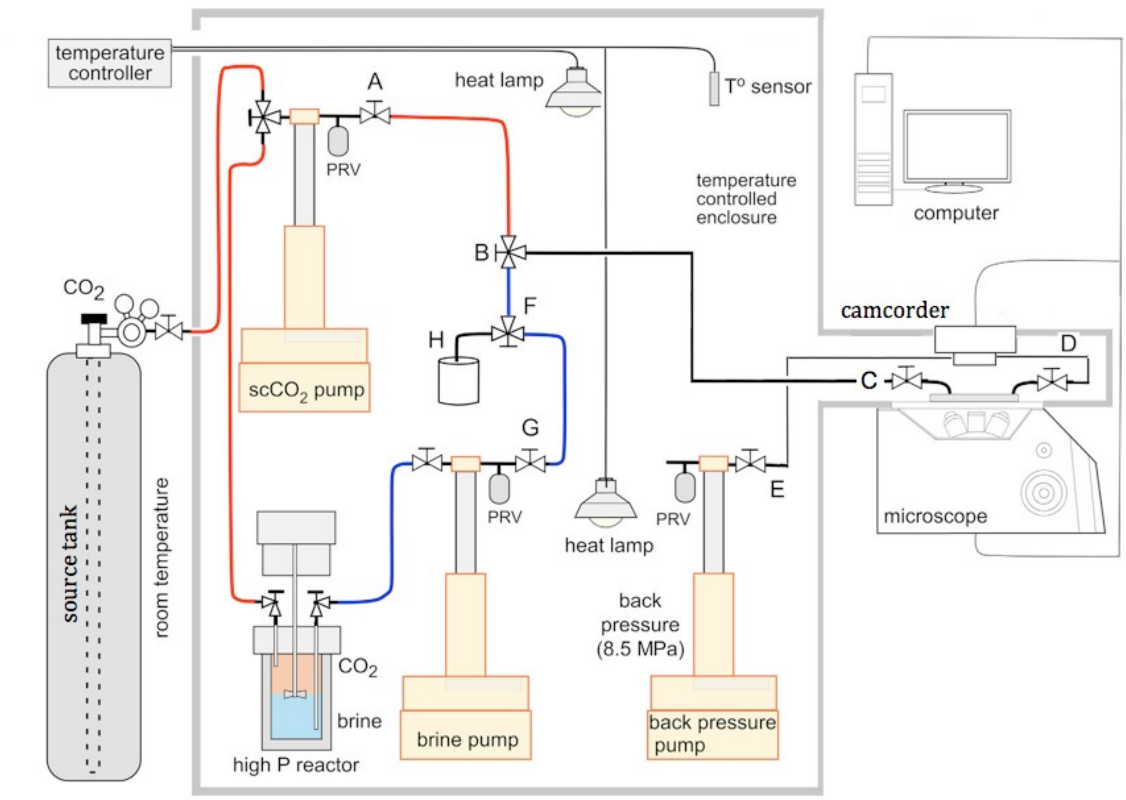

Figure 2. Schematic of the experimental setup for $scCO_2$ injection and brine drainage tests.

2.4 Image analysis

Imaging was performed using an inverted microscope (Carl Zeiss, Observer Z1.m) equipped with a CCD camera (Carl Zeiss, Axiocam MRc5) that records images at the pore scale, and a Sony FDR-AX100 4K camcorder installed over the stage of the inverted microscope to record images at the pore-network scale. Segmentation and analysis of the images were conducted using ImageJ - public domain JAVA based software (Rasband, 1997–2019). Because efficient and direct segmentation of $scCO_2$ from brine and solid posts is difficult, the following steps were applied to the raw images: the raw images taken during a displacement test were first subtracted from the image taken at the initially water-saturated condition, followed by a median and a bilateral filtering (Chaudhury et al., 2011) of the resulting images. A threshold value was then unambiguously determined for each image to distinguish $scCO_2$ phase from others. More details on the process and superimposed image comparing the contours before and after segmentation are presented in Figure S3 of the SI. We manually drew the contour of the $scCO_2$ phase in the original subdomain (3.8×3.7 mm^2, as shown in Figure S3(a), also identical to Figure 5(d)) and calculated the pore space area occupied by $scCO_2$. By comparison with the segmented image in Figure S3(d), we showed errors $< 1\%$, which mostly originated from the edges and connectivities in the narrow pore throats. The resulting binary images were then used to present the displacement characteristics and calculate $scCO_2$ saturation in the water-wet and two mixed-wet micromodels.

3. Results and discussion

In this section, we first present the contact angle measured for $scCO_2$-brine and mixed-wet patterns after coating treatment in Section 3.1, followed by $scCO_2$ saturation and distribution at injection rates varying from $logCa = -8.1$ to -4.4 in the water-wet and two mixed-wet 2.5-D micromodels in Sections 3.2 and 3.3. In Section 3.4, we further quantify the flow characteristics and topological $scCO_2$ distribution in different micromodels at the pore- and pore-network scale. In Section 3.5, the classic *logCa -logM* diagram is presented and the impacts of pore geometry and mixed-wettability are discussed. We finally discuss the experimental implications on spatial variations of CO_2 saturation in a typical GCS site in Section 3.6.

3.1 Contact angle and mixed-wet patterns after treatment

The contact angle was measured for $scCO_2$-brine at 8.5 MPa and 45°C. Both of the untreated water-wet and treated mixed-wet micromodel were initially brine-saturated, followed by $scCO_2$ injection at a low rate until the $scCO_2$-brine distribution in the micromodel was stable with time. The valves connecting to the inlet and outlet of the micromodel were then closed for 12 hours, and microscope images were taken at different locations of the pore network to measure $scCO_2$-brine contact angles on solid posts. Menisci of $scCO_2$-brine interface were selected such that each meniscus possessed a flat contact line of sufficient length so that the change in post geometry and surface roughness did not considerably affect the contact angle measurements. Figure 3(a) presents an example of the microscope image showing the variability of contact angle between $scCO_2$ (white) and brine (gray) in the treated micromodel (marked by the white dashed rectangle in Figure 3(d)). Within the local pore network domain of 2.6×1.9 mm^2, the contact angle varies considerably, from 27° to

119°, indicating a mixed-wet system. This wide variation in contact angle is attributed to the non-uniform flow of coating solution during treatment. Bypassed patches filled by EG may retain originally water wet where coating is difficult to establish. Figure 3(b) further compares the contact angles obtained from over 60 menisci selected within the entire pore network. In the untreated micromodel, the values vary from 20° to 35°. With an average value of 27°± 4°, the untreated micromodel shows a strong water-wet surface, similar to that reported by Hu et al. (2017b), who measured the average contact angle of $scCO_2$-brine at 20° in a micromodel made of the same silica glass. It should be noted that their silica posts were fabricated with circular and smooth surfaces. The slightly higher contact angle measured in our micromodel may be attributed to the rough surface of the glass posts and associated contact line pinning. Figure 3(b) also shows considerable increases in the average contact angle and variations of contact angles after coating treatment. The contact angles after treatment vary from 34° to 145°, with an average value of 89°± 28°. Note the menisci were selected over the entire pore network. This variation in contact angle indicates the spatial heterogeneity in wettability, ranging from strongly water-wet to strongly CO_2-wet (Iglauer et al., 2015). This pore space heterogeneous wetting to brine results in different $scCO_2$ invasion characteristics, which are presented in detail in Section 3.3.

Figure 3. (a) A microscope image showing wide varieties of contact angles between $scCO_2$ (white) and brine (gray) within a local pore domain (indicated by the white dashed rectangle in (d)) after OTS treatment. (b) The contact angle measurements from over 60 selected menisci within the pore network for both untreated and treated micromodels. The quasi-steady state distribution of dyed EG (red color) in the micromodel after OTS injection at (c) $logCa = -7.2$, and (d) $logCa = -3.9$. OTS coating solution was injected from the left side of the micromodel as indicated by the blue arrow. The white arrow in (c) denotes the narrow intermediate-wet choke point established after OTS treatment.

Note that we measured the contact angle of menisci where both $scCO_2$ and brine were present. We assume the wettability of pore space invaded by coating solution during treatment is altered to non-wetting, and that saturated with EG retains its original water-wet surface characteristic. The assumptions were supported through measuring over 60 $scCO_2$-brine menisci present within the pore space previously invaded by the coating solution or saturated by EG (see Figure 3b). We will provide more evidence and discussion by comparing the mixed-wettability patterns vs. CO_2 distribution in Section 3.4.

The distributions of dyed EG (red color) after treatment are shown in Figure 3(c) and 3(d), while the invaded coating solution and silica posts are presented non-fluorescent in blue to black color. The saturation of coating solution in the pore network is 0.50 and 0.70 at low (Figure 3(c)) and high (Figure 3(d)) injection rate, resulting in different areas that had wetting-altered pore surfaces. The average length and standard deviation of EG clusters after area-weighted in Figure 3(c) were measured as 2560 μm and 1870 μm, while the values are ~1/3 at 870 μm and 596 μm in Figure 3(d). It should be noted that when the OTS solution advanced beyond the capillary barrier, it channeled through the relatively open pore domain outlined by the blue frame (Figures 1a. and 1c). By making the pore surfaces in this more open domain intermediate-wet, it became a location where invading $scCO_2$ flow was focused after passing through the capillary barrier. Once through this location, $scCO_2$ flow diverged as discussed later. Thus, this intermediate-wet region behaves as a choke point for $scCO_2$ invasion (see more details in Section 3.3).

The treated and untreated water-wet (WW) micromodels with identical geometry were then used in the $scCO_2$ injection tests. For simplicity, we define (1) the capillary mixed-wet (CM) micromodel as the model was established at a low injection rate of coating solution (Figure 3(c)), where the intermediate-wet patches were capillary-force induced and heterogeneously distributed in the pore network; and (2) the viscous mixed-wet (VM) micromodel as the model was established at a high injection rate of coating solution (Figure 3(d)), where the intermediate-wet patches were viscous-force induced and uniformly distributed in the pore network.

3.2 $scCO_2$ saturation and distribution in the 2.5-D water-wet (WW) micromodel

Figure 4(a) shows the quasi-steady state $scCO_2$ distributions after displacement in the WW micromodel. The corresponding displacement rates (*logCa*) and CO_2 saturations are presented in the parentheses. Depending on injection rates, the injected $scCO_2$ volumes at steady state range from 3 PVs at $logCa = -8.1$ to 200 PVs at $logCa = -4.4$. The overall $scCO_2$ flow characteristics with varying displacement rates are distributed across the classic fingering regimes, i.e., capillary fingering dominates at low displacement rate ($logCa < -6.4$), where $scCO_2$ flows in forward and lateral flow paths with large clusters of entrapped water; viscous fingering develops at large displacement rate ($logCa > -6.1$), where $scCO_2$ widely invades the pore network and displaces water in the form of multiple narrow and well-connected flow paths. At intermediate rates ($logCa = -6.4$ and -6.1), crossover from capillary to viscous fingering is shown by the coexistence of distributed capillary fingering (near the upstream) and concentrated viscous fingering (near the downstream), similar to the experimental observations from Wang et al. (2012), Ferer et al. (2004) and pore-network simulations by Lenormand et al. (1988).

Differing from above studies in a 2-D micromodel, however, we observe the great impacts of 2.5-D heterogeneity of pore geometry on $scCO_2$ distribution. As shown in Figure 4(a) and for most cases (*logCa* <−5.1), $scCO_2$ invades the open slots (marked by the white circles) of the transverse barrier (see Figure 1(a)) that are close to the top and bottom boundaries, and bypasses the barrier and even some slots in center (marked by the red circles). The half-depth barrier hinders longitudinal $scCO_2$ flow in the center and enhances transverse flow that bypasses the slots in front. We selected a local pore domain located by the red box in Figure 4(a) to better understand and discuss the $scCO_2$ flow in Section 3.4.1. At *logCa* ≥ −5.1, $scCO_2$ invades most of the slots under the strong viscous force. The capillary blockage of $scCO_2$ and flow direction changes at a local pore domain are enhanced by the depth-reduced pore throat, comparing to that in a 2-D micromodel that possesses a constant pore throat depth.

3.3 $scCO_2$ saturation and distribution in the 2.5-D mixed-wet micromodels

The fingering flow patterns and CO_2 saturations in the two mixed-wet micromodels are presented in Figures 4(b) and 4(c). The classic flow regime transition from capillary fingering through crossover to viscous fingering can also be observed. At low injection rates (log*Ca*=

−8.1 and −7.4), CO_2 saturations are ~0.65 and ~0.50 in the VM and CM micromodel, but at the crossover zone (log*Ca*= −6.4), the values decrease to 0.49 and 0.42. Further increasing the injection rates in both micromodels results in continuous increase of CO_2 saturations to a similar value of 0.80 at maximum log*Ca*= −4.4. The dependence of CO_2 saturation on solid surface wettability can be deduced from the 30 displacement tests in the three micromodels. For instance, at low injection rates where the flow regime is dominated by capillary fingering (−8.1 ≤ log*Ca*< −6.4), CO_2 saturation in the VM micromodel is 0.12 to 0.14 higher than that in the WW micromodel (see Figures 4(a) and 4(c)), while the value in the CM micromodel is 0.03 lower at log*Ca* = −8.1, and 0.05 to 0.07 higher at log*Ca*= −7.1 and −6.8. The saturation enhancement reaches maximum of 0.18 and 0.12 in the VM and CM micromodels at the intermediate-rate injections, where the flow regime is dominated by crossover from capillary to viscous fingering (log*Ca*= −6.4 and −6.1). At higher rates (log*Ca*> −6.1), the effect of wettability and pore geometry is suppressed by strong viscous force, resulting in high CO_2 saturation in the three micromodels at the maximum injection rate. The overall higher CO_2 saturation in the two mixed-wet micromodels at log*Ca*≤ −6.1 is attributed to the lower capillary entry pressure in pore networks having solid surfaces more wetting to the displacing $scCO_2$, similar to previous observations from Cottin et al. (2011), Zhao et al. (2016) and Hu et al. (2017a).

We show in Figure 4 that more CO_2 saturation enhancement occurs in the VM micromodel than that in the CM. In the two micromodels having identical pore geometry, the lower saturation enhancement in the CM micromodel can be attributed to effectively less area converted to hydrophobic surfaces relative to the VM micromodel. These converted hydrophobic surfaces, at the same time, are more heterogeneously distributed within the pore network (see Figure 2(a) and 2(b)), resulting in higher variations of capillary entry pressure among local pores/pore throats. The heterogeneously distributed hydrophobic surfaces then enhance channelized $scCO_2$ flow and hinder $scCO_2$ displacement efficiency. The non-uniform displacement and preferential CO_2 flow in micromodels and rock cores subject to pore- and sub-core scale heterogeneity has been extensively reported (Krevor, et al., 2011; Shi et al., 2011; Pini et al., 2012; Berg & Ott, 2012; Berg et al., 2013; Chang et al., 2013, 2014; Chen et al., 2018). In a previous study, we presented in four centimeter-scale micromodels the change of CO_2 saturations by a factor of ~10 at similar imposed displacement rates, depending on the heterogeneity and anisotropy of pore networks (Chang et al., 2019b). We show here the importance of mixed wettability and its effect on displacement efficiency and CO_2 saturation, particularly at low displacement rates. In reservoirs where the flow rate is relatively slow ($Ca < 10^{-7}$) and displacement is dominated by capillary fingering, CO_2 storage efficiency may be collectively dependent on pore geometry, solid surface wettability and their heterogeneity.

Different CO_2 distributions in the two mixed-wet pore network are also shown in Figure 4. In the CM micromodel and at $\log Ca < -4.4$, the open slots invaded and bypassed by $scCO_2$ were spatially mixed (see the mixed white and red circles in Figure 4(b)), differing from that in the WW micromodel (see Figure 4(a)). More importantly, at intermediate-rate injections ($-6.8 \leq \log Ca \leq -5.4$), we observed a single $scCO_2$ flow path developed at the barrier downstream (marked by the white arrows in Figure 4(b)). Lower and higher injection rates resulted in additional flow paths around it. This single flow path gradually developed into several dendritic paths towards the outlet. The unique $scCO_2$ flow pattern can be attributed to the preferential $scCO_2$ flow through the narrow intermediate-wet (instead of geometrically induced) choke point marked by the white arrow in Figure 2(a) and bounded by the blue rectangles in Figure 1(a) and 1(c). In the VM micromodel with more uniformly distributed intermediate-wet patches, $scCO_2$ broadly invaded the pore network with well-connected flow paths, except for a bypassed water body at the bottom left corner (see Figure 4(c) at $\log Ca < -6.1$). No significant blockage from the transverse capillary barrier was observed, regardless of flow rate.

Figure 4. The quasi-steady state $scCO_2$ (shown in green) distribution after displacement in the micromodel of (a) water-wet (WW), (b)

capillary mixed-wet (CM) and (c) viscous mixed-wet (VM). The numbers in the parentheses are *logCa* values and CO_2 saturations, respectively. $scCO_2$ is injected at the left side of these images, as indicated by the blue arrow. The circles refer to the open slots in Figure 1c invaded (white) and bypassed (red) by $scCO_2$. The white arrows in (b) indicate the constrained $scCO_2$ flow induced by the narrow intermediate-wet choke point. The red boxes in (a), (b) and (c) mark the local pore domains selected for analyzing pore-scale drainage characteristics and mixed-wettability effects in Figure 5 at *logCa*= −6.4.

In addition to the local choke point, we compare the mixed-wet patterns vs. $scCO_2$ distribution in the entire pore network by overlapping Figure 4(b) at *logCa*=−8.1, −6.1 and −4.4 with Figure 3(c), and Figure 4(c) at *logCa*=−8.1, −6.1 and −4.4 with Figure 3(d). The resulting images (see more details in Figure S4 of the SI) show 70% of $scCO_2$ in the CM pore network distributes within the intermediate-wet patches at *logCa*=−8.11, while the value in the VM pore network is 60%, indicating a more uniform CO_2 distribution among the water-wet and intermediate-wet patches. Both values decrease with increasing injection rates to 50% at*logCa*= −4.4, when compact invasion dominates under strong viscous force regardless of heterogeneities in surface wettability and pore geometry. We do not expect or see exactly the same flow patterns even under the same experimental conditions, as the randomness of pore size and grain surface, as well as the randomness of interfacial velocity at local pores/ pore throats (Kataok et al., 1986). Most of the time we use (lumped) saturation, pressure data and statistics (e.g., the skeleton analysis here) to investigate the fundamental processes. We think we have sufficient reproducibility to distinguish the different flow regimes and mixed-wet impacts as shown by Figure S2 of the SI.

3.4 Quantifications on $scCO_2$ flow characteristics

In this section, we quantify the $scCO_2$ flow characteristics that were descriptive in previous studies (e.g., Lenormand, et al., 1988; Zhang et al, 2011b; Wang et al., 2012), and discuss the effects of mixed-wettability at both pore and pore-network scales. The pore-scale analysis focuses on a local pore domain at 3.8 × 3.7 mm^2 in vicinity of the capillary barrier (indicated by the red squares in Figure 4). Quantification of the pore-network-scale flow characteristics was applied to all the displacement tests in the three micromodels.

3.4.1 Pore-scale $scCO_2$ flow characteristics

Figure 5(a) depicts the selected local pore domain composed of (1) ~100 solid posts (shown in black), (2) large pores 40 μm deep (shown in yellow) and (3) tight pore throats 20 μm deep (shown in red). The average pore and pore-throat size is measured as 204 μm and 80 μm, respectively from Figure 5(g). The porosity is 0.44, similar to the entire pore network. Figure 5(d) represents the $scCO_2$ flow paths (in white color) after displacement within the WW domain at log*Ca*= −6.4. As shown in the figure, $scCO_2$ invades the pore domain from the top left and the bottom right corner (see the red arrows), transversely flows through the domain along the red dotted arrows and flows out of the domain along the blue arrows. Note the bulk flow direction is from left to right. The blockage of $scCO_2$ by the capillary barrier occurs, resulting in flow direction changes and bypass of tight (only 20 μm deep) pore throats. After injection, CO_2 saturation in the WW domain is stable at 0.43. The OTS-altered intermediate-wet patches and CO_2 distribution in the CM and VM domains are also compared for *logCa*= −6.4, and shown in white in Figures 5(b), 5(c), and Figures 5(e) and 5(f), respectively. The steady-state CO_2 saturation after displacement is 0.43 and 0.62, respectively in the CM and VM domain, among which 90% and 64% distributes within the intermediate-wet patches.

The mixed-wettability changes the $scCO_2$ saturation distribution vs. pore/pore throat size in Figure 5(h), which is obtained from aligning Figure 5(d), 5(e) and 5(f) with Figure 5(g). For all the three domains, the majority of $scCO_2$ distributes in large pores/pore throats at 80 to 400 μm, with less than 1% in the tight pore throats (< 80 μm diameter and 20 μm deep). The tight pore throats account for 3% of the pore space in the domain and the pore network. We also observe (1) similar correlations in the WW and CM domains, while a higher CO_2 saturation distribution occurs in smaller pores (< 200 μm diameter) in the VM domain (the accumulative CO_2 saturation in these small pores is 0.29 in the VM domain, while the value is 0.15 in the WW and CM); (2) larger saturation variations in large pores (>300 μm) in the CM domain (note the more irregular red plot). These are consistent with Figure 5(d), 5(e) and 5(f), and indicate different topologies of $scCO_2$ flow path, i.e., better interconnections of flow in large and small pores/pore throats in the VM domain, and more constrained flow in the CM domain with bypass of small pore throats and even large pores.

Characterizing $scCO_2$ distribution topology is important for understanding its invasion into pore networks and ultimately to help predict $scCO_2$ plume shape in reservoirs. We apply a skeleton analysis in the same local pore domain using an Analyze Skeleton plugin in ImageJ to better quantify the topology of $scCO_2$ flow paths and impacts of mixed-wettability. The skeleton geometry is defined as a thin version of that geometry which is equidistant to its boundaries. The binary images of $scCO_2$ phase in the three types of pore domains (Figures 5 (d), (e), (f)) are first skeletonized in ImageJ and illustrated by branches and junctions shown in Figure 5(i), 5(j) and 5(k). A branch is composed of slab pixels that have exactly 2 neighbor pixels, while a junction is defined as the intersection of multiple (more than two) branches, i.e., the junction pixels have more than 2 neighbors. More details on the terminology and method are provided in Arganda-

Carreras et al. (2010). The numbers of branches and junctions, as well as the average branch length for $scCO_2$ flow paths were calculated and listed in Table 2. Also shown in Table 2 are values for the pore domain. The branch numbers increase from 61 in the CM to 135 in the WW, and reach maximum at 221 in the VM domain. Correspondingly, the junction number increases from 29 in the CM to 67 in the WW, and reaches maximum at 110 in the VM domain. Conversely, the average branch length is shortest in the VM and longest in the CM domain. These indicate a more interconnected flow topology of $scCO_2$ after displacement in the VM domain, and a more channelized $scCO_2$ flow in the CM domain. The average branch length of $scCO_2$ flow paths in the WW domain is 226 μm, which is close to the value of the pore domain (240), indicating a flow characteristic dominated by pore geometry.

730

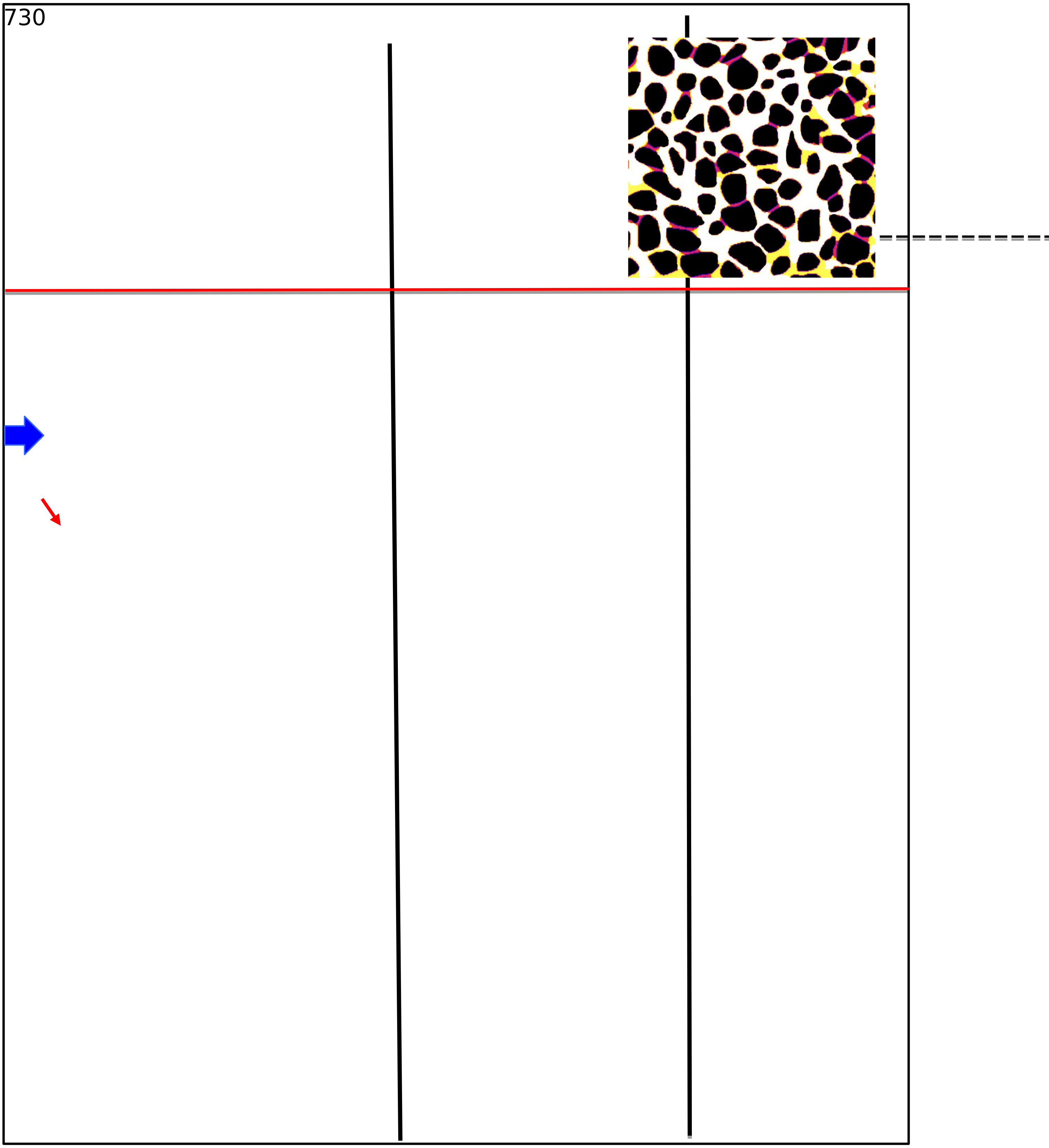

Figure 5. $scCO_2$ flow characteristics and mixed-wet effects through a topological skeleton analysis over a local pore domain (3.8 × 3.7 mm^2). (a) Pore characteristics of the originally WW domain, with full-depth (40 μm) pores shown in yellow and half-depth (20 μm) pore throats in red (these color indicators are also applied to (b), (c), (d), (e) and (f)). (b) and (c) show the mixed-wet patterns in the CM and VM domains, with water-wet pore space shown in yellow and intermediate-wet pore space in white. (d), (e) and (f) present the quasi-steady state $scCO_2$ (in white) distribution in the WW, CM and VM domains, respectively. The red dotted arrows indicate the $scCO_2$ flow directions within the domain, along with red solid arrows for entrance and blue solid arrows for exit. (g) and (h) are the pore size distribution and CO_2 saturation distribution vs. pore/ pore throat size within the pore domain quantified by the Local Thickness plugin in ImageJ software.

(i), (j) and (k) show the skeletonized CO_2 distribution composed by branches and

junctions in different pore domains.

$scCO_2$ distribution

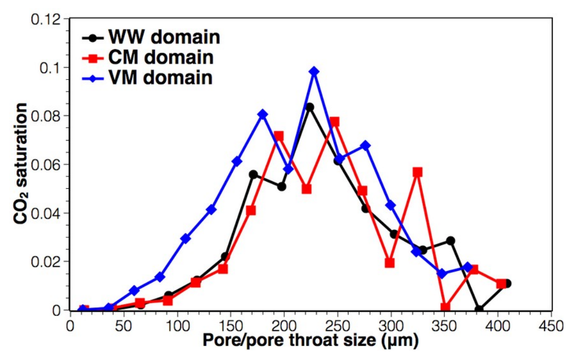

Skeletonized $scCO_2$ flow path

Table 2. The branch and junction number, and average branch length for $scCO_2$ flow at *logCa*= −6.4 and the selected pore domain by a skeleton analysis

Topological characteristics of $scCO_2$ flow paths			
Wetting type	**Number of branches**	**Number of junctions**	**Average branch length (μm)**
CM	61 (0.22)	29 (0.18)	389 (1.62)
WW	135 (0.48)	67 (0.42)	226 (0.94)
VM	221 (0.79)	110 (0.69)	194 (0.81)
Topological characteristics of pore domain			
	280	158	240

Note: The numbers in the parentheses are specific values calculated from ratios between $scCO_2$ flow paths and pore domain for Number of branches, Number of junctions and Average branch length.

Figure 6. The specific branch and junction number, and specific branch length vs. *logCa* in the WW, CM and VM micromodel.

3.4.2 Pore-network-scale flow characteristics

We applied the topological analysis to the three micromodels to investigate $scCO_2$ flow characteristics at the pore-network scale. The branch and junction number, and the average branch length for $scCO_2$ flow paths (N_b,N_j and L), and for the pore networks ($N_{b,m}$, $N_{j,m}$ and L_m) were first calculated, and their ratios, defined as specific branch number, specific junction number and specific branch length are presented as a function of *logCa* in Figure 6. In the WW micromodel, the branch and junction numbers that keep relatively high plateau values at $logCa<-6.5$ (black lines Figure 6(a) and 6(b)) correspond to the wide invasion and randomly distributed forward and lateral flow paths observed in the capillary fingering regime. The considerable reduction in branch and junction numbers at $logCa=-6.4$ and −6.1 is consistent with the crossover from capillary to viscous fingering and decreased displacement efficiency. At higher injection rates ($logCa>-6.1$) where viscous fingering dominates the flow regime, the branch and junction numbers increases with new developed and interconnected flow paths. The variation of the specific branch length as a function of *logCa* (Figure 6(c)) is generally mirrored to specific branch and junction number vs. *logCa*. This is expected as flow paths develop interconnected, the branch and junction number increase whereas the average branch length decreases.

Figure 6 also presents the largest branch and junction numbers in the VM micromodel among the three. This is in favor of GCS by increasing displacement efficiency. The CM micromodel yields longest branch length and lowest branch and junction number. In mixed-wet caprocks, the channelized flow developed within the intermediate-wet patches may increase capillary leakage of $scCO_2$ accumulation below because of the locally reduced capillary entry pressure.

3.5 CO_2 saturation vs. capillary number considering mixed wettability

Figure 7(a) presents the relations between CO_2 saturation and *logCa* for the displacement experiments conducted in the three wetting types of micromodels. An alternative definition of capillary number ($Ca^{¿}$) from Lenormand et al. (1988) that considers the solid surface wettability is calculated as follows:

$$Ca^{¿} = (\mu \times \bar{u}) / (\sigma \times \acute{\cos}\theta), \qquad \text{Eq. (2)}$$

Where $\acute{\cos}\theta$ is derived from the pore space area (A) and average contact angle of the water-wet and intermediate-wet patches:

$$\acute{\cos}\theta = \frac{A_1 \cos\theta_1 + A_2 \cos\theta_2}{A_1 + A_2} \qquad \text{Eq. (3)}$$

For the CM micromodel, $\theta_1 = 27°$, $A_1/(A_1+A_2) = 0.50$; $\theta_2 = 89°$, $A_2/(A_1+A_2) = 0.50$; for the VM micromodel, $\theta_1 = 27°$, $A_1/(A_1+A_2) = 0.30$; $\theta_2 = 89°$, $A_2/(A_1+A_2) = 0.70$. For the original WW micromodel, $\theta_1 = \theta_2 = 27°$. The

CO_2 saturation vs. $\log Ca^{¿}$ relations for the three micromodels are shown by colored plots in Figure 7(a), which translate rightward from the CO_2 saturation – *logCa* relations at 0.4 unit in the CM and 0.6 unit in the VM micromodel. In the WW micromodel, the two plots overlap without considerable change due to the small contact angle. These correspond to the fact that the presence of intermediate-wet rock surfaces (larger contact angles) further assures viscous fingering within the near-field network and transition to the capillary fingering regime occurs closer to the injection well. The $Ca^{¿}$ that consider solid surface wettability may be able to better quantify the fingering and crossover flow regimes. However, caution is needed as variations of contact angles and their spatially heterogeneous distributions are likely to be more complex in natural reservoirs formations than in the two treated micromodels.

Figure 7(b) illustrates the classic $\log Ca^{¿}$– $\log M$ diagram, with boundaries of different displacement patterns from Lenormand et al. (1988) shown in gray and Zhang et al. (2011) in dash lines. The different boundaries observed from the two studies were attributed to the different pore geometries and pore-size variations. The values of $\log Ca^{¿}$ and $\log M$ used in this study are shown by solid symbols. In a previous study (Chang et al., 2019b), we conducted $scCO_2$ displacement experiments at 40 °C and 9 MPa in (1) an anisotropic and homogeneous micromodel consisting of elliptical silicon posts, with estimated transverse-to-longitudinal permeability ratio of 0.63; (2) a heterogeneous sandstone-analogue micromodel, which was patterned based on section micrographs of a Mt. Simon sandstone core extracted from the injection well of the Illinois Basin - Decatur project (Senel et al., 2014). We include data on the two micromodels (hollow symbols) and refer them as #R1 and #R3 in the figure. Under similar conditions at 41°C and 9.0 MPa, Wang et al. (2012) conducted scCO_2 displacement tests in a homogeneous isotropic pore network that consisted of 200 μm cylindrical silicon posts, 120 μm pore bodies and 26.7 μm pore throats. Their results were shown and referred as #R2 in Figure 7(b) (see more detailed images on the referred micromodels in Figure S5 of the SI). All the referred data were obtained in micromodels with water-wet solid surfaces (θ=15°) and similar pore/pore throat depth (35 to 37 μm). We tried to include as much data as possible for better comparison, however, were hindered by the narrow capillary number range applied in previous studies, particularly by the deficiency at low rates ($\log Ca$¿< -7.0) that are dominant at GCS sites.

The colored arrows in Figure 7(b) indicate the flow regime crossover with minimum CO_2 saturation observed in each study. The crossover *logCa* values in this and referred studies, regardless of pore geometries or surface wettabilities, ranges from −5.6 to −6.6, generally lower than the boundaries (−4.6 to −5.8) predicted by Zhang et al. (2011) at a similar $\log M$ value of −1.34. The displacing fluid (dodecane) viscosity from Zhang et al. (2011), however, is almost two orders of magnitude higher at 1.35 mPa·s than that of $scCO_2$ used in this study, while the interfacial tension (IFT) between the displacing and resident fluid (polyethylene glycol 200) is lower at 13.87 mN/m. The low $scCO_2$ viscosity and high IFT with brine may intensify interfacial instability for $scCO_2$-brine displacement and result in lower $\log Ca$ values for flow regime changes from capillary fingering to crossover. In a 2-D homogeneous micromodel, Armstrong & Berg (2013) showed that individual pore drainage events occurred at an intrinsic rate, which was independent of bulk flow rate. Further modeling results indicated the two-phase interfacial velocity increased with decreasing viscosity of the displacing phase or increasing interfacial tension and for the same capillary number, the velocity of two-phase interface can differ by an order of magnitude or more (Armstrong et al., 2015). The broad distribution in *Ca* associated with crossover (minimum nonwetting phase saturation indicated by arrows in Figure 7(b)) suggests that capillary number alone does not explain the pore-scale displacement. While most studies focus on the fingering flow regimes and transitions using fluid pairs of different viscosity ratios (Dong et al., 2011; Zhang et al., 2011a,b; Dehoff et al., 2012; Wang et al., 2012; Liu et al., 2013; Zheng et al., 2017), additional studies are required using fluid pairs of same viscosity ratio but different in displacing fluid viscosities or IFTs.

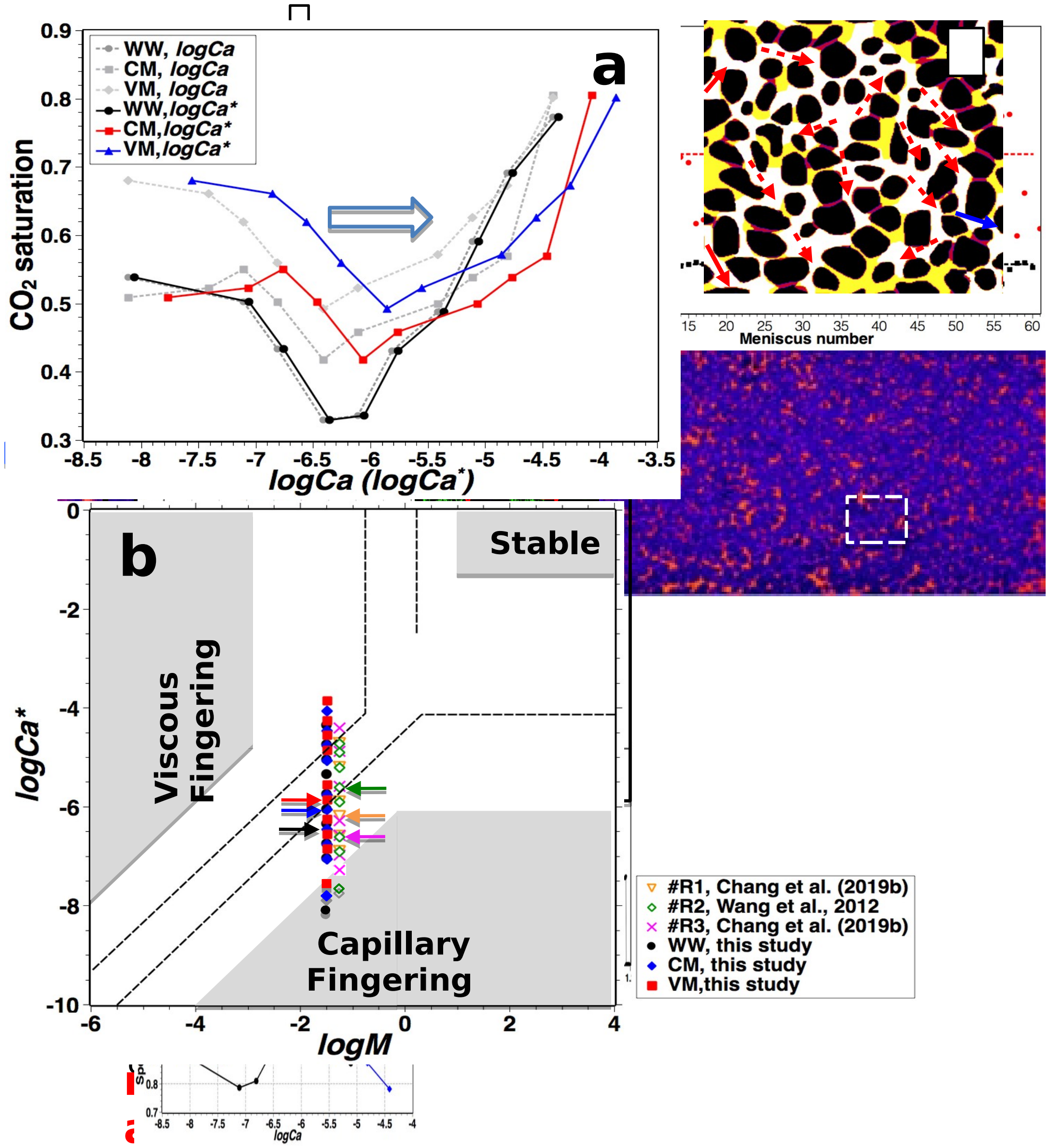

Figure 7. **(**a) The correlations of CO_2 saturation vs. *logCa* (the gray dash lines) and CO_2 saturation vs. $\log Ca^{¿}$ (the colored solid lines) for the displacement experiments conducted in the three wetting

types of micromodels. The blue arrow indicates the shift direction of $\log Ca$¿ from $log Ca$. (b) $\log Ca$¿– $log M$ stability diagram showing three stability areas and the locations of the displacement experiments in this and previous studies for scCO_2 and water. The dash lines are the stability boundaries from Zhang et al. (2011b) and the gray zones denote the stability areas from Lenormand et al. (1988). The colored arrows mark the conditions at saturation minimum in each study.

3.6 Field implications

The 30 tests under the wide range of displacement rates allowed investigations on the full spectrum of fingering flow regimes, CO_2 saturations, and mixed-wettability impacts. These results have implications for a GCS site. In Figure 8, we show CO_2 saturation vs. distance to the injection well calculated from the typical CO_2 flow velocity in a GCS site. We assume (1) at the field, CO_2 is injected at a volumetric rate (Q) of 10,000 m^3/d over a screen length of 15 m, and (2) scCO_2 density (ρ) from reservoir pressure and temperature is close to that at experimental conditions and CO_2 velocities in the formation is radially uniform. This volumetric rate corresponds to an annual injection of one million metric tonnes of CO_2 at 8.5 MPa and 45 °C (this study), and 1.8 million metric tones of CO_2 at 9 MPa and 40 °C (Wang et al., 2012; Chang et al., 2019b). The distance from the injection well can then be calculated as follows:

$$d = \frac{Q}{2\pi h \bar{u}} \quad \text{Eq. (4)}$$

Where d refers to the (radial) distance to the injection well, h is the screen length of the injection well, and $\bar{u}$ is the CO_2 velocity that equals to the lab values listed in Table 1.

Results from Wang et al. (2012) and Chang et al. (2019b) in Micromodel #R1, #R2, #R3 and #R4 were also included in Figure 8, with estimated CO_2 saturations from their published figures. #R4 refers to an anisotropic and homogeneous micromodel that consists of elliptical silicon posts with estimated transverse-to-longitudinal permeability ratio of 6.86 (see Figure S5 for more details in the SI). #R4 also possesses water-wet solid surface (θ=15°) and constant pore/pore throat depth at 37 μm. CO_2 saturations after displacement in this micromodel showed high values (~0.90) over the applied injection rates, with no crossover flow observed.

In the three micromodels of identical geometry, CO_2 saturation varies as a function of distance to the injection well, depending on the wettability. Comparing to the WW micromodel, VM enhances CO_2 saturation over the investigated distance up to 130 m away from the injection well, while CM only enhances the value at locations 0.25 to 25 m away. In the WW and two mixed-wet micromodels, the crossover from viscous to capillary fingering occurs at locations close to the injection well (1.27 to 2.50 m), and the two mixed-wet systems accelerate the saturation rebound to saturation plateau. For the seven micromodels investigated, viscous fingering flow dominates the constrained locations < 1 m away from the injection well, imposing a very limited impact on the storage efficiency at the field. This again indicates that laboratory experiments at low injection rates are important for obtaining more field-relevant implications.

Figure 8 also indicates the great impact of pore-network anisotropy and heterogeneity on CO_2 saturation. As shown in the figure, pore-network anisotropy imposes the most pronounced effect on CO_2 saturation. The anisotropic Micromodel #R4 with high transverse-to-longitudinal permeability ratio (6.86:1) results in highest CO_2 saturations, while the anisotropic Micromodel #R1 with low transverse-to-longitudinal permeability ratio (0.63:1) yields lowest CO_2 saturations at 0.10 to 0.40. The pore size surprisingly does not have a considerable impact on CO_2 saturation at locations > 20 m away from the injection well, when comparing Micromodel #R2 with Micromodel #R3 and the 2.5-D heterogeneous WW micromodel in this study. A higher CO_2 saturation was expected in Micromodel #R2 containing large 120 μm pore and in the WW micromodel with an average pore size of 190 μm. The average pore size of Micromodel #R3 is smaller at 33 μm. Note the small pore depth relative to pore size in #R2 and the WW micromodel, which may limit the displacement efficiency since (1) Wang et al. (2012) observed the transition of $scCO_2$ flow from widely distributed forward and lateral flow paths to one gradually narrowing finger leading to the outlet and bypass the major pore domain by the small variations of pore depth in Micromodel #R2, and (2) we observed the preferential flow of CO_2 through the deep open slots in the transverse capillary barrier and bypass the majority of pore domain downstream in the WW micromodel. The effect of depth variation is weakened in Micromodel #R3 due to the similar pore size and depth. We emphasis here the importance of pore/pore throat depth in determining two-phase flow and saturation, and suggest careful consideration of the third dimension during micromodel design and fabrication.

It is noted that results from this and previous studies were obtained in centimeter-scale micromodels that possess pore size variations in a range of tens to hundreds of micrometers. Great caution is needed in using these laboratory results for understanding field-scale GCS behavior (e.g., predicting the CO_2 saturation vs. distance to the injection well using Figure 8) because heterogeneities and gravity are important at the larger scale. In the field, the viscous/capillary $scCO_2$ fingers may coincide with high-permeability channels developed at the meter to kilometer scale, while local pore structures and small fingers may become secondary in affecting the $scCO_2$ plume (Birkholzer et al., 2015). In addition, gravity could not be considered in these laboratory experiments on horizontal pore networks. The interplay between viscous/capillary fingering and gravity are also important as gravity is dominant in shaping 3-D plumes and increasing leakage potential through the caprock (Zhou & Birkholzer, 2011; Trevisan et al., 2017).

Figure 8. CO_2 saturation vs. distance from the injection well (in logarithmic scale) for the displacement experiments conducted in the three micromodels and in Wang et al. (2012) and Chang et al. (2019b)

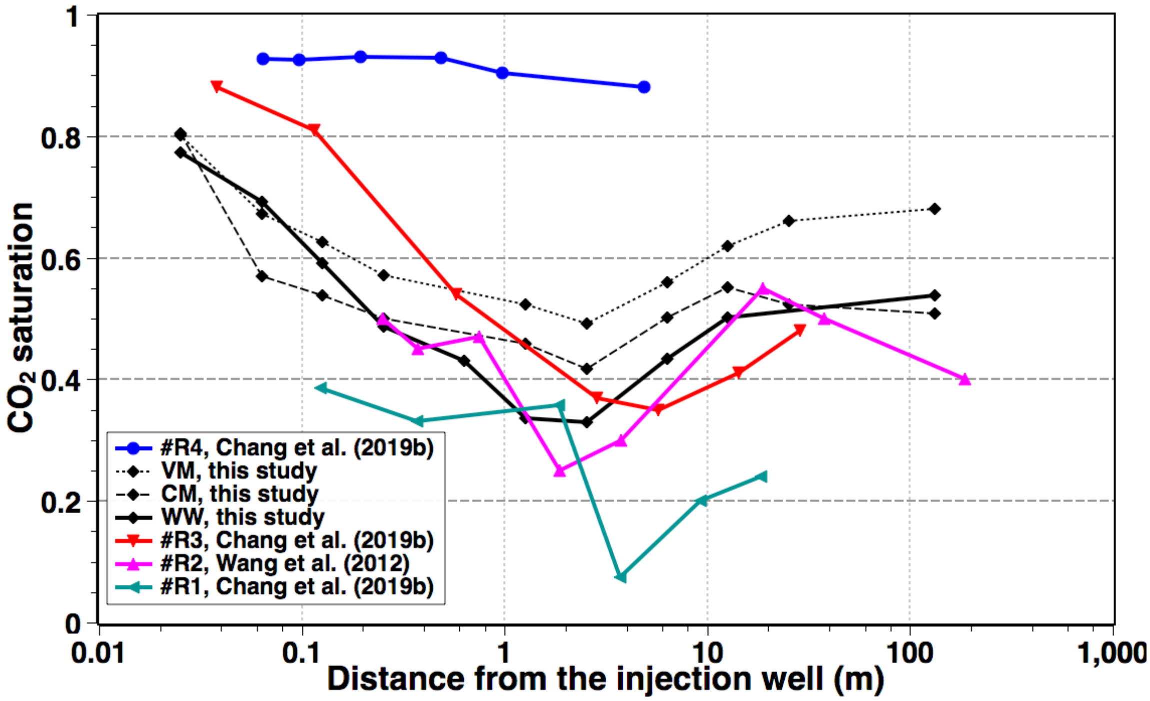

using different pore networks under similar experimental conditions.

4. Conclusions

Secure and efficient CO_2 storage in a geological formation can be affected by the mixed-wettability of reservoir rocks, and therefore this characteristic requires a systematic investigation. By applying a coating solution to modify wettability in a 2.5-D micromodel, we created two mixed-wet systems, one viscous force-induced resulting in uniformly distributed intermediate-wet patches; and one capillary force-induced resulting in heterogeneously distributed intermediate-wet patches. The two mixed-wet and the originally water-wet micromodels were then compared in $scCO_2$ injection experiments. A full spectrum of flow-regime transition from capillary fingering through crossover to viscous fingering was observed in the three micromodels. The pronounced effects of 2.5-D heterogeneity of pore network on $scCO_2$ distribution and saturation were indicated by (1) $scCO_2$ preferential flow along the large 40 μm deep pores and bypass of tight 20 μm deep pore throats, and (2) the comparisons between micromodels with varying pore characteristics. A detailed analysis on CO_2 saturation and topological distribution showed (1) high storage efficiency and wide interconnections of CO_2 flow paths in reservoirs containing more and uniformly distributed intermediate-wet and water-wet patches, and (2) hindered storage efficiency and channelized CO_2 flow paths in reservoirs containing heterogeneously distributed intermediate-wet patches. The channelized flow of $scCO_2$ (especially at locations close to injection well) may increase leakage potential through caprock. This pore-network-scale study indicates the importance of mixed-wettability in determining CO_2 storage efficiency and spatial variation in depleted hydrocarbon reservoirs and others that may present mixed-wet rock surface.

Supporting Information (SI)

More detailed information on the contact angle measurements, characterizations on the drainage flow regimes and referred micromodels are provided in the SI.

Conflicts of interest

The authors declare no competing financial interest.

Acknowledgements

This material was based upon the work supported by the U.S. Department of Energy, Office of Science, Office of Basic Energy Sciences, Energy Frontier Research Centers program under Contract no. DE-AC02-05CH11231. We appreciate the valuable comments provided by the reviewers and the Associate Editor, which helped improve presentation of this work. Data are deposited in the Dryad repository with DOI: 10.7941/D14P62, and available through the following link during the review process: https://datadryad.org/stash/share/MMmArpl0nxIOdS2jO4VF0dFWi9NLFHFB2HzoYx9EGSc.

References

Al-Khdheeawi, E., Vialle, S., Sarmadivaleh, M., Barifcani, A., & Iglauer, S. (2017). Impact of reservoir wettability and heterogeneity on CO_2 plume migration and trapping capacity. *Int. J. Greenhouse Gas Control*, 58, 142−158.

Anderson, W. G. (1987a). Wettability literature survey—part 4: effects of wettability on capillary pressure. *J. Petrol. Technol.*, 39 (10), 1283–1300.

Anderson, W.G. (1987b). Wettability literature survey Part 6: the effects of wettability on water flooding. *J. Petrol. Technol.*, 39 (12), 1605–1622.

Arganda-Carreras, I., Fernandez-Gonzalez, R., Munoz-Barrutia, A., & Ortiz-De-Solorzano, C. (2010). 3D reconstruction of histological sections: Application to mammary gland tissue. *Microsc. Res. Tech.*, 73 (11), 1019–1029.

Armstrong, R. T., & Steffen, B. (2013). Interfacial velocities and capillary pressure gradients during Haines jumps. *Phys. Rev. E*, 88(4), 600–614.

Armstrong, R. T., Georgiadis, A., Ott, H., Klemin, D., & Berg, S. (2014). Critical capillary number: desaturation studied with fast X-ray computed microtomography. *Geophys. Res. Lett.* 41, 55–60.

Bachu, S., & Bennion, B. (2007). Effects of in-situ conditions on relative permeability characteristics of CO_2-brine systems. *Environ. Geol.*, 54

(8), 1707–1722.

Berg, S., & Ott, H. (2012). Stability of CO_2–brine immiscible displacement. *Int. J. Greenhouse Gas Control*, 11, 188–203.

Berg, S., Oedai, S., & Ott, H. (2013). Displacement and mass transfer between saturated and unsaturated CO_2–brine systems in sandstone. *Int. J. Greenhouse Gas Control*, 12, 478–492.

Birkholzer, J. T., Zhou, Q., & Tsang, C. (2009). Large-scale impact of CO_2 storage in deep saline aquifers: A sensitivity study on pressure response in stratified systems. *Int. J. Greenhouse Gas Control*, 3 (2), 181–194.

Birkholzer, J. T., Oldenburg, C. M., & Zhou, Q. (2015). CO_2 migration and pressure evolution in deep saline aquifers. *Int. J. Greenhouse Gas Control*, 40, 203–220.

Broseta, D., Tonnet, N., & Shah, V. (2012). Are rocks still water-wet in the presence of dense CO_2 or H_2S? *Geofluids*, 12, 280–294.

Chang, C., Zhou, Q., Xia, L., Li, X., & Yu, Q. (2013). Dynamic displacement and non-equilibrium dissolution of supercritical CO_2 in low permeability sandstone: An experimental study. *Int. J. Greenhouse Gas Control*, 14, 1–14.

Chang, C., Zhou, Q., Guo, J., & Yu, Q. (2014). Supercritical CO_2 dissolution and mass transfer in low-permeability sandstone: Effect of concentration difference in water-flood experiments. *Int. J. Greenhouse Gas Control*, 28, 328–342.

Chang, C., Zhou, Q., Kneafsey, T. J., Oostrom, M., Wietsma, T. M., & Yu, Q. (2016). Pore-scale supercritical CO_2 dissolution and mass transfer under imbibition conditions. *Adv. Water Resour.*, 92: 142–158.

Chang, C., Zhou, Q., Oostrom, M., Kneafsey, T. J., & Mehta, H. (2017). Pore-scale supercritical CO_2 dissolution and mass transfer under drainage conditions, Adv. Water Resour., 100, 14–25.

Chang, C., Zhou, Q., Kneafsey, T. J., Oostrom, M., & Ju, Y. (2019a). Coupled supercritical CO_2 dissolution and water flow in pore-scale micromodels. *Adv. Water Resour.*, 123, 54–69.

Chang, C., Kneafsey, T. J., Zhou, Q., Oostrom, M., & Ju, Y. (2019b). Scaling the impacts of pore-scale characteristics on unstable supercritical CO_2-water drainage using a complete capillary number. *Int. J. Greenhouse Gas Control*, 86, 11–21.

Chaudhury, K. N., Sage, D., & Unser, M., (2011). Fast O(1) bilateral filtering using trigonometric range kernels, *IEEE Trans. Image Process*, 2(12), 3376–3382.

Chen, Y., Li, Y., Valocchi, A. J., & Christensen, K. T. (2018). Lattice Boltzmann simulations of liquid CO_2 displacing water in a 2D heterogeneous micromodel at reservoir pressure conditions. *J. Contam. Hydrol.*, 212, 14–27.

Chiquet, P., Daridon, J. L., Broseta, D. & Thibeau, S. (2007). CO_2/water interfacial tensions under pressure and temperature conditions of CO_2 geological storage. *Energy Convers. Manage.,* 48, 736–744.

Cihan, A., Birkholzer, J. T., & Zhou, Q. (2013). Pressure buildup and brine migration during CO_2 storage in multilayered aquifers. *Ground Water*, 51(2), 252–267.

Cottin, C., Bodiguel, H., & Colin, A. (2010). Drainage in two-dimensional porous media: from capillary fingering to viscous flow. *Phys. Rev. E*, 82 (4), 046315.

Cottin, C., Bodiguel, H., & Colin, A. (2011). Influence of wetting conditions on drainage in porous media: A microfluidic study. *Phys. Rev. E*, 84(2), 026311.

DeHoff, K. J., Oostrom, M., Zhang, C., & Grate, J. W. (2012). Evaluation of two-phase relative permeability and capillary pressure relations for unstable displacements in a pore network, *Vadose Zone J.*, 11(4), doi:10.2136/vzj2012.0024.

Doughty, C. (2010). Investigation of CO_2 Plume Behavior for a Large-Scale Pilot Test of Geologic Carbon Storage in a Saline Formation. *Transp. Porous Media*, 82 (1), 49–76.

Dong, B., Yan, Y., & Li, W. (2011). LBM simulation of viscous fingering phenomenon in immiscible displacement of two fluids in porous media. *Transp. Porous Media*, 88(2), 293–314.

Fathi, S. J., Austad, T., & Strand, S. (2010). Wettability Alteration in Carbonates: The Effect of Water-Soluble Carboxylic Acids in Crude Oil. *Energ. Fuels*, 24, 2514− 2519.

Ferer, M., Ji, C., Bromhal, G. S., Cook, J., Ahmadi, G., & Smith, D. H.

(2004). Crossover from capillary fingering to viscous fingering for immiscible unstable flow: Experiment and modeling. *Phys. Rev. E*, 70 (1), 016303.

Goodwin, D. G., Xia, Z., Gordon, T. B., Gao, C., Bouwer, E. J., & Fairbrother, D. H. (2016). Biofilm development on carbon nanotube/ polymer nanocomposites. *Environ. Sci.: Nano*, 3, 475-684.

Goodman, A., Hakala, A., Bromhal, G., Deel, D., Rodosta, T., Frailey, S., Small, M., Allen, D., Romanov, V., Fazio, J., et al. (2011). U.S. DOE methodology for the development of geologic storage potential for carbon dioxide at the national and regional scale. *Int. J. Greenhouse Gas Control*, 5 (4), 952−965.

Gribanova, E.; Molchanova, L.; Grigorov, O.; Porova, V. pH dependence of contact angles on glass and quartz. *Colloid J. USSR* 1976, 38, 504−506.

Hildebrand, T., & Rüesgsegger, P. (1996). A new method for the model-independent assessment of thickness in three-dimensional images. *J of Microscopy*, 185, 67−75.

Hilfer, R., & Øren, P. E. (1996). Dimensional analysis of pore scale and field scale immiscible displacement. *Transp. Porous Med.*, 22, 53–72.

Hu, R., Wan, J., Kim, Y., & Tokunaga, T. K. (2017a). Wettability effects on supercritical CO_2-brine immiscible displacement during drainage:

Pore-scale observation and 3D simulation, *Int. J. Greenhouse Gas Control*, 60, 129–139.

Hu, R., Wan, J., Kim, Y., & Tokunaga, T. K. (2017b). Wettability impact on supercritical CO_2 capillary trapping: Pore-scale visualization and quantification, *Water Resour. Res.* **2017b**, 53, 6377–6394, doi:10.1002/2017WR020721.

Huq, F., Haderlein, S. B., Cirpka, O. A., Nowak, M., Blum, P., & Grathwohl, P. (2015). Flow-through experiments on water–rock interactions in a sandstone caused by CO_2 injection at pressures and temperatures mimicking reservoir conditions. *Appl. Geochem.*, 58, 136-146

Iglauer, S., Pentland, C., Bush, A. (2015). CO_2 wettability of seal and reservoir rocks and the implications for carbon geosequestration. *Water Resour. Res.*, 51, 729–774. https://doi.org/10.1002/2014WR015553.

IPCC. (2005). Special report on carbon dioxide capture and storage. In: Metz, B., Davidson, O., de Coninck, H.C., Loos, M., Meyer, L.A. (Eds.), Prepared by Working Group III of the Intergovernmental Panel on Climate Change. Cambridge University Press, Cambridge, United Kingdom and New York, NY, USA.

Juanes, R., MacMinn, C. W., & Szulczewski, M. L. (2010). The footprint of the CO_2 plume during carbon dioxide storage in saline aquifers: Storage efficiency for capillary trapping at the basin scale. *Transp. Porous Media*, 82 (1), 19-30.

Jung, J. W., & Wan, J. (2012). Supercritical CO_2 and ionic strength effects on wettability of silica surfaces: Equilibrium contact angle measurements. *Energ. Fuels*, 26(9), 6053–6059. https://doi.org/10.1021/ef300913t.

Kataok, I., Ishii, M., Serizawa, A. (1986). Local formulation and measurements of interfacial area concentration in two-phase flow. *Int. J. Multiph.*, 12 (4), 505–529.

Karadimitriou, K. N., Mahani, H., Steeb, H. & Joekar-Niasar, V. (2019). Non-monotonic effects of salinity on wettability alteration and two-phase flow dynamics in PDMS micromodels. *Water Resour. Res.*, https://doi.org/10.1029/2018WR024252.

Kim, Y., Wan, J., Kneafsey, T. J., & Tokunaga, T. K. (2012). Dewetting of silica surfaces upon reactions with supercritical CO_2 and Brine: Pore scale studies in micromodels. *Environ. Sci. Technol.*, 46 (7), 4228−4235.

Kovscek, A. R., Wong, H., & Radke, C. J. (1993). A pore-level scenario for the development of mixed wettability in oil reservoirs. *AIChE J.*, 39, 1072−1085. https://doi.org/10.1002/aic.690390616.

Krevor, S. C. M., Pini, R., Li, B., & Benson, S. M. (2011). Capillary heterogeneity trapping of CO_2 in a sandstone rock at reservoir conditions. *Geophys. Res. Lett.*, 38, L15401, doi:10.1029/2011GL048239.

Levine, J. S., Goldberg, D. S., Lackner, K. S., Matter, J. M., Supp, M. G., & Ramakrishnan, T. S. (2014). Relative permeability experiments of carbon dioxide displacing brine and their implications for carbon sequestration, *Environ. Sci. Technol.*, 48(1), 811–818.

Lenormand, R., Touboul, E., & Zarcone, C. (1988). Numerical models and experiments on immiscible displacements in porous media. *J. Fluid Mech.*, 189, 165–187.

Liu, H., Valocchi, A. J., Kang, Q., & Werth, C. (2013). Pore-scale simulations of gas displacing liquid in a homogeneous pore network using the Lattice Boltzmann method, *Transp. Porous Media*, 99(3), 555–580.

Lv, P., Liu, Y., Wang, Z., Liu, S., Jiang, L., Chen, J., & Song, Y. (2017). In Situ local contact angle measurement in a CO_2–brine–sand system using microfocused X-ray CT. *Langmuir*, 33, 3358–3366.

MacMinn, C. W., Szulczewski, M. L., & Juanes, R. (2010). CO_2 migration in saline aquifers. Part 1. Capillary trapping under slope and groundwater flow. *J. Fluid Mech.*, 662 (7), 329–351.

MacMinn, C. W., Szulczewski, M. L., & Juanes, R. (2011). CO_2 migration in saline aquifers. Part 2. Capillary and solubility trapping. *J. Fluid Mech.*, 688, 321–351.

Moebius, F., & Or, D. (2014). Pore scale dynamics underlying the motion of drainage fronts in porous media. *Water Resour. Res.*, 50, 8441–8457.

Morrow, N. R. (1990). Wettability and its effect on oil recovery. *J. Petrol. Technol.*, 42 (12), 1476–1484.

Nordbotten, J. M., Celia, M. A., & Bachu, S. (2005). Injection and Storage of CO_2 in Deep Saline Aquifers: Analytical Solution for CO_2 Plume Evolution During Injection. *Transp. Porous Media*, 58 (3), 339–360.

Park, D. S., Upadhyay, J., Singh, V., Thompson, K. E., & Nikitopoulos, D. E. (2015). Fabrication of 2.5D Rock-Based Micromodels with High Resolution Features*. ASME 2015 International Mechanical Engineering Congress and Exposition*, p V010T13A014.

Pini, R., Krevor, S. C. M., & Benson, S. (2012). Capillary pressure and heterogeneity for the CO_2/water system in sandstone rocks at reservoir conditions. *Adv. Water Resour*., 38, 48–59.

Rasband, W. S. (1997–2019). ImageJ, U.S. National Institutes of Health, Bethesda, Maryland, USA, https://imagej.nih.gov/ij/.

Rücker, M., Bartels, W. B., Singh, K., Brussee, N., Coorn, A., van der Linde, H. A., Bonnin, A., Ott, H., Hassanizadeh, S. M., Blunt, M. J., Mahani, H., Georgiadis, A., & Berg, S. (2019). The effect of mixed wettability on pore-scale flow regimes based on a flooding experiment in Ketton limestone. *Geophys. Res. Lett.*, 46, 3225–3234. https://doi.org/10.1029/2018GL081784.

Saffman, P. G., & Taylor, G. (1958). The penetration of a fluid into a porous medium or Hele-Shaw cell containing a more viscous liquid. *Proc. R. Soc. A*, 245, 312-329.

Salathiel, R. A. (1973). Oil recovery by surface film drainage in mixed-wettability rocks. *J. Petrol. Technol.*, 25, 1216–1224.

Sanchez-Vila, X., Dentz, M., & Donado, L. D. (2007). Transport-controlled reaction rates under local non-equilibrium conditions, *Geophys. Res. Lett.*, 34,L10404, doi:10.1029/2007GL029410.

Seyyedi, M., Sohrabi, M., & Farzaneh, A. (2015). Investigation of rock wettability alteration by carbonated water through contact angle measurements. *Energ. Fuels*, 29, 5544−5553.

Senel, O., Will, R., & Butsch, R. J. (2014). Integrated reservoir modeling at the Illinois Basin – Decatur Project. *Greenhouse Gases: Sci. Technol.*, 4 (5), 662–684.

Shi, J. Q., Xue, Z., & Durucan, S. (2011). Supercritical CO_2 core flooding and imbibition in Tako sandstone-influence of sub-core scale heterogeneity *Int. J. Greenhouse Gas Control*, 5, 75−87.

Tokunaga, T. K., Wan, J., Jung, J. W., Kim, T. W., Kim, Y., & Dong, W. (2013). Capillary pressure and saturation relations for supercritical CO_2 and brine in sand: High-pressure $P_c(S_w)$ controller/meter measurements and capillary scaling predictions, *Water Resour. Res.*, 49, 4566–4579, doi:10.1002/wrcr.20316.

Trevisan, L., Pini, R., Cihan, A., Birkholzer, J. T., Zhou, Q., Gonzalez-Nicolas, A., & Illangasekare, T. H. (2017). Imaging and quantification of spreading and trapping of carbon dioxide in saline aquifers using meter-scale laboratory experiments. *Water Resour. Res.*, 53 (1), 485–502, doi:10.1002/2016WR019749.

Tsang, C. F., Birkholzer, J., Rutqvist, J. (2008). A comparative review of hydrologic issues involved in geologic storage of CO2 and injection disposal of liquid waste, *Environ. Geol.*, 54, 1723–1737, doi:10.1007/s00254-007-0949-6.

Tsakiroglou, C. D., & Avraam, D. G. (2002). Fabrication of a new class of porous media models for visualization studies of multiphase flow processes. *J. Mater. Sci.*, 37, 353. doi:10.1023/A:1013660514487.

Wan, J., Tokunaga, T. K, Tsang, C. F., Bodvarsson, G. S. (1996). Improved glass micromodel methods for studies of flow and transport in fractured porous media, *Water Resour. Res.*, 32, 1955–1964.

Wang, S., & Tokunaga. T. K. (2015). Capillary pressure-saturation relations for supercritical CO_2 and brine in limestone/dolomite sands: Implications for geologic carbon sequestration in carbonate reservoirs. *Environ. Sci. Technol.*, 49, 7208−7217.

Wang, S., Edwards, I. M., Clarens, A. F. (2013), Wettability phenomena at the CO_2-brine-mineral interface: Implications for geologic carbon sequestration, *Environ. Sci. Technol.*, 47(1), 234–241.

Wang, Y., Zhang, C., Wei, N., Oostrom, M., Wietsma, T. W., Li, X., & Bonneville, A. (2012). Experimental study of crossover from capillary to viscous fingering for supercritical CO_2–water displacement in a homogeneous pore network. *Environ. Sci. Technol.*, 47, 212–218.

Xu, B., Yortsos, Y. C., & Salin, D. (1998). Invasion percolation with viscous forces. *Phys. Rev. E*, 57, 739–751.

Xu, K., Bonnecaze, R., & Balhoff, M. (2017a). Egalitarianism among bubbles in porous media: an ostwald ripening derived anticoarsening phenomenon. *Phys. Rev. Lett.*, 119 (26), 264502.

Xu, K., Liang, T., Zhu, P., Qi, P., Lu, J., Huh, C., & Balhoff, M. (2017b). A 2.5-D glass micromodel for investigation of multi-phase flow in porous media. *Lab Chip*, 17, 640–646.

Yang, D. Y., Gu, Y. G., & Tontiwachwuthikul, P. (2008). Wettability determination of the reservoir brine−reservoir rock system with dissolution of CO_2 at high pressures and elevated temperatures. *Energ. Fuels*, 22 (1), 504−509.

Yun, W., Ross, C.M., Roman, S., & Kovscek, A. R. (2017). Creation of a dual-porosity and dual-depth micromodel for the study of multiphase flow in complex porous media. *Lab Chip*, 17 (8), 1462−1474.

Zarikos, I. M., Hassanizadeh, S. M., van Oosterhout, L. M., & van Oordt, W. (2018). Manufacturing a Micromodel with Integrated Fibre Optic

Pressure Sensors. *Transp. Porous Media*, https://doi.org/10.1007/s11242-018-1202-3.

Zhao, B., MacMinn, C. W., & Juanes, R. (2016). Wettability control on multiphase flow in patterned microfluidics. *Proc. Natl. Acad. Sci. U.S.A.*, 113 (37), 10251–10256.

Zhang, C., Oostrom, M., Grate, J. W., Wietsma, T. W., & Warner, M. G. (2011a). Liquid CO_2 displacement of water in a dual-permeability pore network micromodel. *Environ. Sci. Technol.*, 45 (17), 7581–7588.

Zhang, C., Oostrom, M., Wietsma, T. W., Grate, J. W., & Warner, M. G. (2011b). Influence of Viscous and Capillary Forces on Immiscible Fluid Displacement: Pore-Scale Experimental Study in a Water-Wet Micromodel Demonstrating Viscous and Capillary Fingering. *Energ. Fuels,* 25 (8), 3493–3505.

Zheng, X., Mahabadi, N., Yun, T. S., & Jang, J. (2017). Effect of capillary andviscous force on CO_2 saturationand invasion pattern in the microfluidic chip. *J. Geophys. Res. Solid Earth*, 122, 1634–1647.

Zhou, Q., & Birkholzer, J. T. (2011). On scale and magnitude of pressure build-up induced by large-scale geologic storage of CO_2. *Greenhouse Gases: Sci. Technol.*, 1(1), 11–20.

Zuo, L., Zhang, C., Falta, R. W., & Benson, S. M. (2013). Micromodel investigations of CO_2 exsolution from carbonated water in sedimentary rocks. *Adv. Water Resour.*, 53, 188–197.

1363